


# Analytical weak-lensing shear response of galaxy model fitting

Xiangchong Li<sup>1\*</sup> ,

<sup>1</sup> Brookhaven National Laboratory, Bldg 510, Upton, New York 11973, USA

Received April 20, 2025; accepted Month ??, 2025

## ABSTRACT

Galaxy model fitting is widely employed to estimate properties such as galaxy shape, size, and color. Understanding how the outputs of galaxy model fitting respond to weak lensing shear distortions is crucial for accurate shear estimation and mitigating shear-related systematics in weak lensing image analyses. In this paper, we investigate how the fitted parameters—specifically flux, size, and shape—respond to weak-lensing shear distortions within the **AnaCal** framework. To achieve this, we introduce *quintuple numbers*, a novel algebraic system inspired by dual numbers from automatic differentiation. Quintuple numbers enable the propagation of shear response information throughout the entire model-fitting process by linking analytical pixel shear responses to those of the fitted parameters. We integrate *quintuple numbers* into the **AnaCal** framework to derive the shear responses of shapes estimated with model fitting and validate the pipeline using image simulations that include realistic blending. Our results demonstrate that the multiplicative bias remains below  $3 \times 10^{-3}$  for ground-based, oversampled images.

**Key words:** gravitational lensing; weak; cosmology; observations; techniques: image processing.

## 1 INTRODUCTION

We are entering an exciting era of precision cosmology, driven by the launch of next-generation astronomical imaging surveys (Peebles & Ratra 2003). These groundbreaking projects aim to rigorously test the prevailing cosmological model and shed light on the accelerated expansion of the Universe. A key observational tool in this endeavor is weak gravitational lensing, which traces the growth of cosmic structure. This phenomenon arises when massive structures bend the light from distant galaxies, introducing subtle, coherent shear distortions in their observed shapes (Bartelmann & Schneider 2001; Kilbinger 2015; Mandelbaum 2018).

Among the most prominent “Stage IV” surveys are the Vera C. Rubin Observatory’s Legacy Survey of Space and Time (LSST, Ivezić et al. 2019), the European Space Agency’s Euclid mission (Laureijs et al. 2011), and NASA’s Nancy Grace Roman Space Telescope (Akeson et al. 2019). To meet the science goals, these programs demand shear measurement techniques with systematic biases controlled at the level of a few tenths of a percent (Massey et al. 2013; The LSST Dark Energy Science Collaboration et al. 2018). Achieving this level of precision requires survey-specific algorithmic solutions tailored to the unique characteristics of each dataset.

Weak gravitational lensing introduces a coherent distortion to galaxy shapes through a remapping of image coordinates. This effect can be described by a Jacobian transformation

that maps the true (source) coordinates  $\beta$  to the observed (image) coordinates  $\theta$  via the lensing potential. In the weak lensing regime, where deflections are small, this mapping can be approximated as a linear transformation:

$$\theta = \mathbf{A} \cdot \beta, \quad \text{where} \quad \mathbf{A} = \begin{pmatrix} 1 - \kappa - \gamma_1 & -\gamma_2 \\ -\gamma_2 & 1 - \kappa + \gamma_1 \end{pmatrix}. \quad (1)$$

Here,  $\kappa$  is the convergence, which magnifies or demagnifies the image, and  $(\gamma_1, \gamma_2)$  are the two components of the shear distortion, which introduce anisotropic stretching. In this paper, we assume  $\kappa = 0$  and focus exclusively on the shear components  $\gamma_1$  and  $\gamma_2$ . In practice, weak lensing measurements rely on statistically extracting the shear  $\gamma$  from the observed ellipticity of many galaxies, under the assumption that their intrinsic shapes are randomly oriented. A key to accurate shear estimation lies in computing the linear shear response of galaxy shape measurements—that is, the first-order derivative of the measured shape with respect to the applied shear (Huff & Mandelbaum 2017). By evaluating this response, one can construct a perturbative solution that relates observed shape distortions to the underlying shear field, enabling shear inference with accuracy at the sub-percent level, even in the presence of complex image systematics.

In recent years, several innovative approaches to weak lensing shear estimation have emerged that reduce or eliminate the need for external image simulations—particularly in the case where blended sources reside at the same redshift. Among these, **METADETECTION** (Sheldon et al. 2020, 2023) stands out for its use of numerical self-calibration, while **AnaCal** (Li & Mandelbaum 2023; Li et al. 2025) introduces a

\* xli6@bnl.gov

fully analytical method for deriving the linear shear response. Thanks to its analytical nature, **AnaCal** is exceptionally efficient: it can compute a shear estimator for a single detected galaxy in under one millisecond. Another promising approach is **BFD** (Bernstein & Armstrong 2014; Bernstein et al. 2016), a Bayesian framework for shear estimation. However, **BFD** currently may require percent-level corrections from simulations to mitigate detection biases, particularly in cases involving galaxy blending. It is worth noting that external simulations may still be necessary to calibrate the redshift distribution of source galaxies when blending occurs between galaxies at different redshifts, each subject to distinct shear distortions (MacCrann et al. 2022). In this paper, we concentrate on correcting shear estimation bias assuming blended sources are from the same redshift, and defer the complexities introduced by multi-redshift blending to future work.

The analytical formalism introduced by Li & Mandelbaum (2023); Li et al. (2024) provides a unified approach for correcting four major sources of shear bias: detection bias, selection bias, galaxy model bias and Point Spread Function (PSF) shape leakage. It achieves accuracy up to second order in shear. The method begins by computing the shear response of each smoothed image pixel value, then propagates these responses to downstream quantities—such as detection likelihood, selection metrics, and shape estimators—using the chain rule of derivatives. This pixel-level formulation allows for a rigorous analytical connection between the underlying shear field and the final shear estimator. Building on this foundation, Li et al. (2025) extend the framework to include a correction for noise bias. This is accomplished by generating synthetic, pure-noise images that replicate the noise characteristics of the observed data, akin to the approach used in metacalibration (Sheldon & Huff 2017). These noise realizations allow the analytical formalism to robustly account for biases introduced by stochastic image noise.

In this paper, we extend the **AnaCal** formalism to derive the shear response of the galaxy model-fitting process. This advancement enables a quantitative understanding of how fitted model parameters—such as galaxy flux, shape, and size—respond to weak lensing shear distortions. To accomplish this, we introduce quintuple numbers, a novel commutative ring structure that allows the automatic propagation of shear responses from the smoothed image pixels (inputs to model fitting) to the model parameters (outputs of the fitting). The quintuple number system is inspired by dual numbers, which are commonly used in automatic differentiation to track first-order derivatives during computation (Gunes Baydin et al. 2015). In analogy, quintuple numbers are designed to carry first-order shear response terms throughout the entire model-fitting process. This allows for a fully analytical and efficient computation of how each model parameter varies with shear, without relying on numerical perturbations or external simulations.

This paper is organized as follows: Section 2 introduces the analytical shear response of model fitting process and develops a shear estimator with Gaussian model fitting. Section 3 presents systematic tests on ground-based image simulations with the observational condition of Hyper Suprime-Cam Survey (Li et al. 2022a). Finally, Section 4 provides a summary and outlook.

## 2 SHEAR RESPONSE OF MODEL FITTING

In this section, we provide a comprehensive overview of our methodology. We begin in Section 2.2 by reviewing the analytical pixel shear response introduced in Li & Mandelbaum (2023) and noise bias correction introduced in Li et al. (2025). In Section 2.3, we introduce the quintuple number system that is utilized to propagate our analytical pixel shear response. Finally, in Section 2.4, we describe a simple model-fitting procedure used for shape estimation, and use quintuple numbers to derive shear response of its output parameters.

### 2.1 PSF and Noise Correction

In this study, we define the observed image smeared by the PSF as  $f_p(\mathbf{x})$ , where  $p(\mathbf{x})$  denotes the PSF model. We assume that the PSF model is both accurate and precise, and we refer readers to (Zhang et al. 2023b; Berlfein et al. 2025) for PSF modelling errors. The Fourier transforms of the observed image and the PSF model are defined as

$$\begin{aligned} f_p(\mathbf{k}) &= \iint d^2x f_p(\mathbf{x}) \exp(-i\mathbf{k} \cdot \mathbf{x}), \\ p(\mathbf{k}) &= \iint d^2x p(\mathbf{x}) \exp(-i\mathbf{k} \cdot \mathbf{x}). \end{aligned} \quad (2)$$

To eliminate the anisotropy in the original PSF and enable the use of the analytical pixel shear response method proposed by Li & Mandelbaum (2023), we transform the PSF into an isotropic Gaussian form. This is achieved by first deconvolving the original PSF and then applying an isotropic Gaussian filter in Fourier space (see Zhang 2008; Huff & Mandelbaum 2017; Sheldon & Huff 2017 for similar procedures). The Gaussian filter, with standard deviation  $\sigma_h$ , is defined as

$$h(\mathbf{k}) = \exp\left(-\frac{k^2 \sigma_h^2}{2}\right), \quad (3)$$

where  $k \equiv |\mathbf{k}|$  is the magnitude of the wave-number vector. As will be shown in Section 2.2, this procedure facilitates the derivation of shear response from the smoothed image.

To remove noise bias in shear estimation, we generate a pure noise image with a different realization but identical statistical properties to the noise in the observed image. This pure noise is then rotated by  $90^\circ$  and added to the observed image to create a renoised version, following the approach of Sheldon & Huff (2017). We denote the Fourier transform of this pure noise as  $n(\mathbf{k})$ , and its deconvolution uses the PSF rotated by  $90^\circ$ , denoted  $p^{90}(\mathbf{k})$ . We then apply the analytical noise bias correction introduced in Li et al. (2025). Specifically, the noise is deconvolved using  $p^{90}(\mathbf{k})$  and then convolved with the Gaussian  $h(\mathbf{k})$ . The resulting renoised, smoothed image is denoted as  $f_h(\mathbf{x})$ , and its Fourier transform is given by

$$f_h(\mathbf{k}) = h(\mathbf{k}) \left( \frac{f_p(\mathbf{k})}{p(\mathbf{k})} + \frac{n(\mathbf{k})}{p^{90}(\mathbf{k})} \right). \quad (4)$$

One limitation of this noise bias correction method is the need to artificially double the image noise prior to detection and measurement. Notably, a recent study by Zhang et al. (2023a) proposes leveraging deep field images from the same survey to mitigate noise effects in such correction schemes. We plan to incorporate the methodology of Zhang et al.

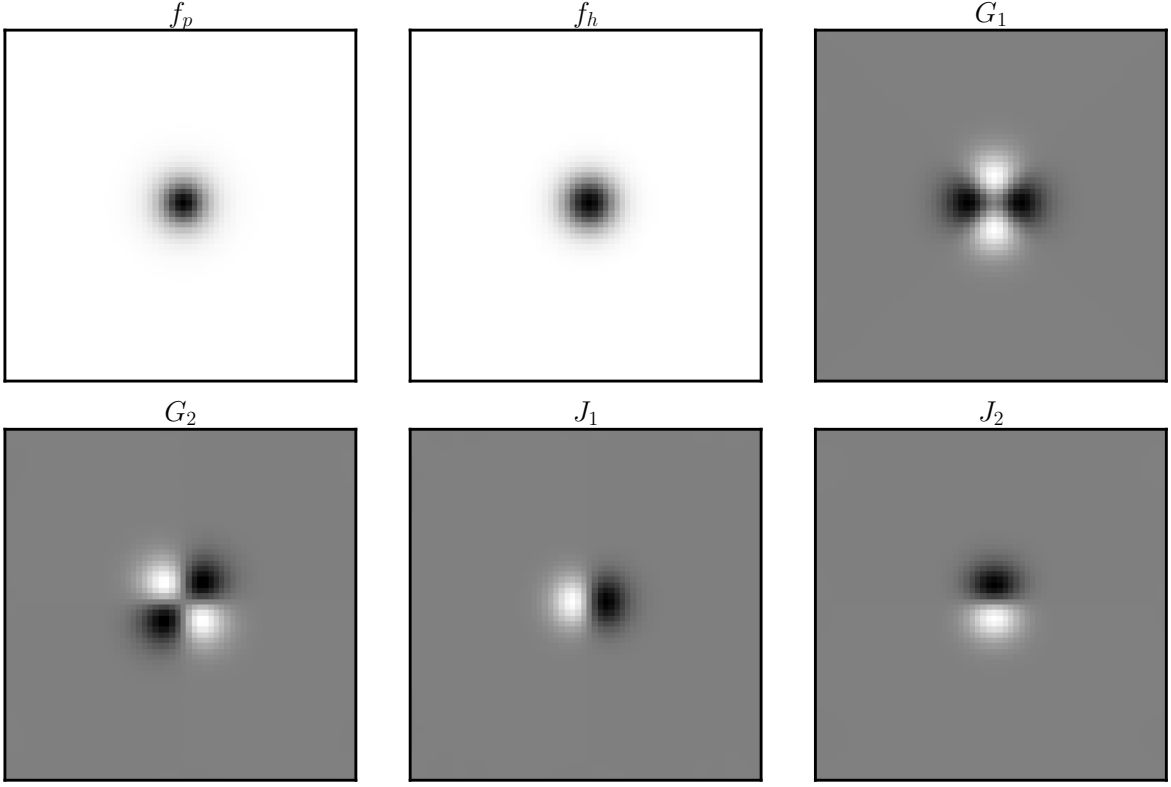


**Figure 1.** We show the noiseless image  $f_p(\mathbf{x})$ , the smoothed image  $f_h(\mathbf{x})$ , and the filtered images ( $G_1(\mathbf{x}), G_2(\mathbf{x}), J_1(\mathbf{x}), J_2(\mathbf{x})$ ), which are key components of the pixel-level shear response (Li & Mandelbaum 2023). The images  $G_1$  and  $G_2$  represent the response of the smoothed image  $f_h(\mathbf{x})$  to small shear distortions along the  $\gamma_1$  and  $\gamma_2$  directions, respectively. In contrast,  $J_1$  and  $J_2$  quantify how this shear response changes with shifts in the reference point about which the shear distortion is applied. The original image has a seeing size (FWHM) of  $0''.80$ , and the FWHM of the Gaussian smoothing kernel is  $0''.85$ .

(2023a) into our analytical shear estimation framework in future work.

## 2.2 Analytical Pixel Shear Response

Li & Mandelbaum (2023) investigated the impact of weak-lensing shear distortions on pixel values that have been smoothed by a Gaussian filter following PSF deconvolution. Their analysis interprets these smoothed pixel values as projections of the signal onto a set of pixel basis functions. The shear response of each pixel values is derived using the analytical shear response of the pixel basis functions. Building upon this framework, Li et al. (2025) derived analytical expressions for the shear response of the renoised image.

In this work, we present the shear response of the smoothed, renoised image directly and refer the reader to Li & Mandelbaum (2023) and Li et al. (2025) for detailed derivations:

$$\begin{aligned} \frac{\partial f_h(\mathbf{x})}{\partial \gamma_1} &= G_1(\mathbf{x}) + x_1 J_1(\mathbf{x}) - x_2 J_2(\mathbf{x}), \\ \frac{\partial f_h(\mathbf{x})}{\partial \gamma_2} &= G_2(\mathbf{x}) + x_2 J_1(\mathbf{x}) + x_1 J_2(\mathbf{x}), \end{aligned} \quad (5)$$

where the auxiliary smoothed images  $G_1$ ,  $G_2$ ,  $J_1$ , and  $J_2$  are

defined as

$$\begin{aligned} G_1(\mathbf{x}) &= \mathcal{F}^{-1} \left[ \left( \frac{f_p(\mathbf{k})}{p(\mathbf{k})} - \frac{n(\mathbf{k})}{p^{90}(\mathbf{k})} \right) h(\mathbf{k}) (k_1^2 - k_2^2) \right], \\ G_2(\mathbf{x}) &= \mathcal{F}^{-1} \left[ \left( \frac{f_p(\mathbf{k})}{p(\mathbf{k})} - \frac{n(\mathbf{k})}{p^{90}(\mathbf{k})} \right) h(\mathbf{k}) (2k_1 k_2) \right], \\ J_1(\mathbf{x}) &= \mathcal{F}^{-1} \left[ \left( \frac{f_p(\mathbf{k})}{p(\mathbf{k})} - \frac{n(\mathbf{k})}{p^{90}(\mathbf{k})} \right) h(\mathbf{k}) k_1 \right], \\ J_2(\mathbf{x}) &= \mathcal{F}^{-1} \left[ \left( \frac{f_p(\mathbf{k})}{p(\mathbf{k})} - \frac{n(\mathbf{k})}{p^{90}(\mathbf{k})} \right) h(\mathbf{k}) k_2 \right], \end{aligned} \quad (6)$$

and  $\mathcal{F}^{-1}(\bullet)$  denotes the inverse Fourier transform. The quantities  $G_1$  and  $G_2$  characterize how the Gaussian PSF profile changes in response to shear distortions along the  $\gamma_1$  and  $\gamma_2$  directions, respectively. The combinations  $x_1 J_1 - x_2 J_2$  and  $x_2 J_1 + x_1 J_2$  describe how the relative positions of neighboring pixels are altered due to the applied shear distortion.  $G_1$ ,  $G_2$ ,  $J_1$ , and  $J_2$  will be used to define quintuple numbers, a commutative ring structure, to automatically propagate shear response to any observables measured from the smoothed, renoised image.

We note that the shear response derived above assumes the origin of the shear distortion is at the coordinate  $(0, 0)$ . If instead we wish to evaluate the shear response relative to a different reference point,  $(x_1^{\text{ref}}, x_2^{\text{ref}})$ , the expressions for the

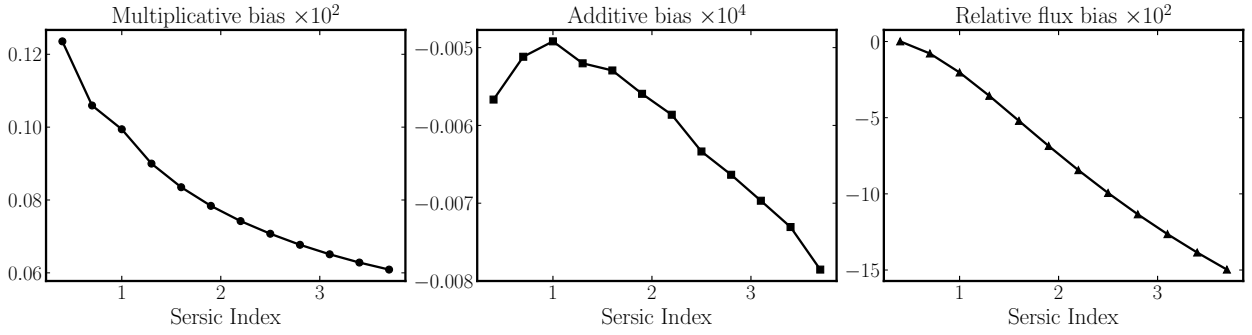


**Figure 2.** The left and middle panels display the multiplicative ( $m_1$ ) and additive ( $c_1$ ) shear estimation biases, respectively, for galaxies with varying Sersic indices. The right panel shows the relative flux bias, defined as the ratio of measured to true flux minus one. Despite using a Gaussian model to fit galaxies with non-Gaussian morphologies—leading to a 15% flux bias—the shear estimation biases remain below the 0.2% level relative to the input shear distortion ( $\gamma_1 = 0.02$ ).

pixel-wise shear response become:

$$\begin{aligned} \frac{\partial f_h(\mathbf{x})}{\partial \gamma_1} &= G_1(\mathbf{x}) + (x_1 - x_1^{\text{ref}})J_1(\mathbf{x}) \\ &\quad - (x_2 - x_2^{\text{ref}})J_2(\mathbf{x}), \\ \frac{\partial f_h(\mathbf{x})}{\partial \gamma_2} &= G_2(\mathbf{x}) + (x_2 - x_2^{\text{ref}})J_1(\mathbf{x}) \\ &\quad + (x_1 - x_1^{\text{ref}})J_2(\mathbf{x}). \end{aligned} \quad (7)$$

In Fig. 1, we present examples of the filtered images of a noiseless galaxy that is used to determine its pixel shear response. The reference origin point of the shear distortion is set to the center of the image.

### 2.3 Response Propagation with Quintuple Number

With the pixel shear response derived in Li & Mandelbaum (2023) and presented in equation (5), we can compute the shear response of any observable measured from the smoothed image by applying the chain rule of derivatives. In Li & Mandelbaum (2023), this pixel-level shear response was used to derive the shear response of FPFs shapes (Li et al. 2018, 2022b)—a fixed-kernel shape estimator based on Shapelets (Refregier 2003; Massey & Refregier 2005). Compared to fixed-kernel estimators, model-fitting methods have higher signal-to-noise ratio; however, they are significantly more complex, often requiring many iterative steps. In principle, the shear response of a model-fitting estimator can also be computed via the chain rule, provided all functions involved are differentiable. However, manually tracing this response through the iterative fitting process is generally intractable due to its complexity. To address this challenge, we introduce quintuple numbers, an extension of dual numbers (Gunes Baydin et al. 2015) used in automatic differentiation, which allows us to propagate shear response automatically through the model-fitting procedure.

We generalize the concept of infinitesimal  $\epsilon$  in dual number (Gunes Baydin et al. 2015) by introducing four distinct infinitesimals,  $\epsilon_1, \epsilon_2, \epsilon_3, \epsilon_4$ , each of which squares to zero. Typically, we also require that products of *different* infinitesimals vanish as well. More formally, we impose:

$$\epsilon_i \epsilon_j = 0 \quad \text{for all } i, j. \quad (8)$$

We then define a quintuple number:

$$q = q_0 + q_1 \epsilon_1 + q_2 \epsilon_2 + q_3 \epsilon_3 + q_4 \epsilon_4. \quad (9)$$

Additionally, it can be expressed as a five-dimensional vector  $(q_0, q_1, q_2, q_3, q_4)$ . Because all products  $\epsilon_i \epsilon_j$  vanish, this five-term expression captures every possible term in the quintuple number.

Below, we give out the basic operation rules between two dual numbers  $q^{(1)} = (q_0^{(1)}, q_1^{(1)}, q_2^{(1)}, q_3^{(1)}, q_4^{(1)})$  and  $q^{(2)} = (q_0^{(2)}, q_1^{(2)}, q_2^{(2)}, q_3^{(2)}, q_4^{(2)})$ .

**Addition:** Addition of two quintuple numbers is performed component-wise:

$$\begin{aligned} q^{(1)} + q^{(2)} &= (q_0^{(1)} + q_0^{(2)}) \\ &\quad + (q_1^{(1)} + q_1^{(2)}) \epsilon_1 + (q_2^{(1)} + q_2^{(2)}) \epsilon_2 \\ &\quad + (q_3^{(1)} + q_3^{(2)}) \epsilon_3 + (q_4^{(1)} + q_4^{(2)}) \epsilon_4. \end{aligned} \quad (10)$$

**Multiplication:** Multiplication of two quintuple numbers uses the distributive law and the fact that any product  $\epsilon_i \epsilon_j$  is zero:

$$\begin{aligned} q^{(1)} \times q^{(2)} &= (q_0^{(1)} q_0^{(2)}) \\ &\quad + (q_0^{(2)} q_1^{(1)} + q_0^{(1)} q_1^{(2)}) \epsilon_1 \\ &\quad + (q_0^{(2)} q_2^{(1)} + q_0^{(1)} q_2^{(2)}) \epsilon_2 \\ &\quad + (q_0^{(2)} q_3^{(1)} + q_0^{(1)} q_3^{(2)}) \epsilon_3 \\ &\quad + (q_0^{(2)} q_4^{(1)} + q_0^{(1)} q_4^{(2)}) \epsilon_4. \end{aligned} \quad (11)$$

**Division:** For division by a non-infinitesimal (i.e. when the real part of the denominator is nonzero), we keep only the first-order terms in each  $\epsilon_i$ :

$$\begin{aligned} \frac{q^{(1)}}{q^{(2)}} &= \frac{q_0^{(1)}}{q_0^{(2)}} \\ &\quad + \left( \frac{q_1^{(1)} q_0^{(2)} - q_1^{(2)} q_0^{(1)}}{q_0^{(2)^2} \right) \epsilon_1 \\ &\quad + \left( \frac{q_2^{(1)} q_0^{(2)} - q_2^{(2)} q_0^{(1)}}{q_0^{(2)^2} \right) \epsilon_2 \\ &\quad + \left( \frac{q_3^{(1)} q_0^{(2)} - q_3^{(2)} q_0^{(1)}}{q_0^{(2)^2} \right) \epsilon_3 \\ &\quad + \left( \frac{q_4^{(1)} q_0^{(2)} - q_4^{(2)} q_0^{(1)}}{q_0^{(2)^2} \right) \epsilon_4 \end{aligned} \quad (12)$$

Here again, we neglect any product of two  $\epsilon_i$ s.

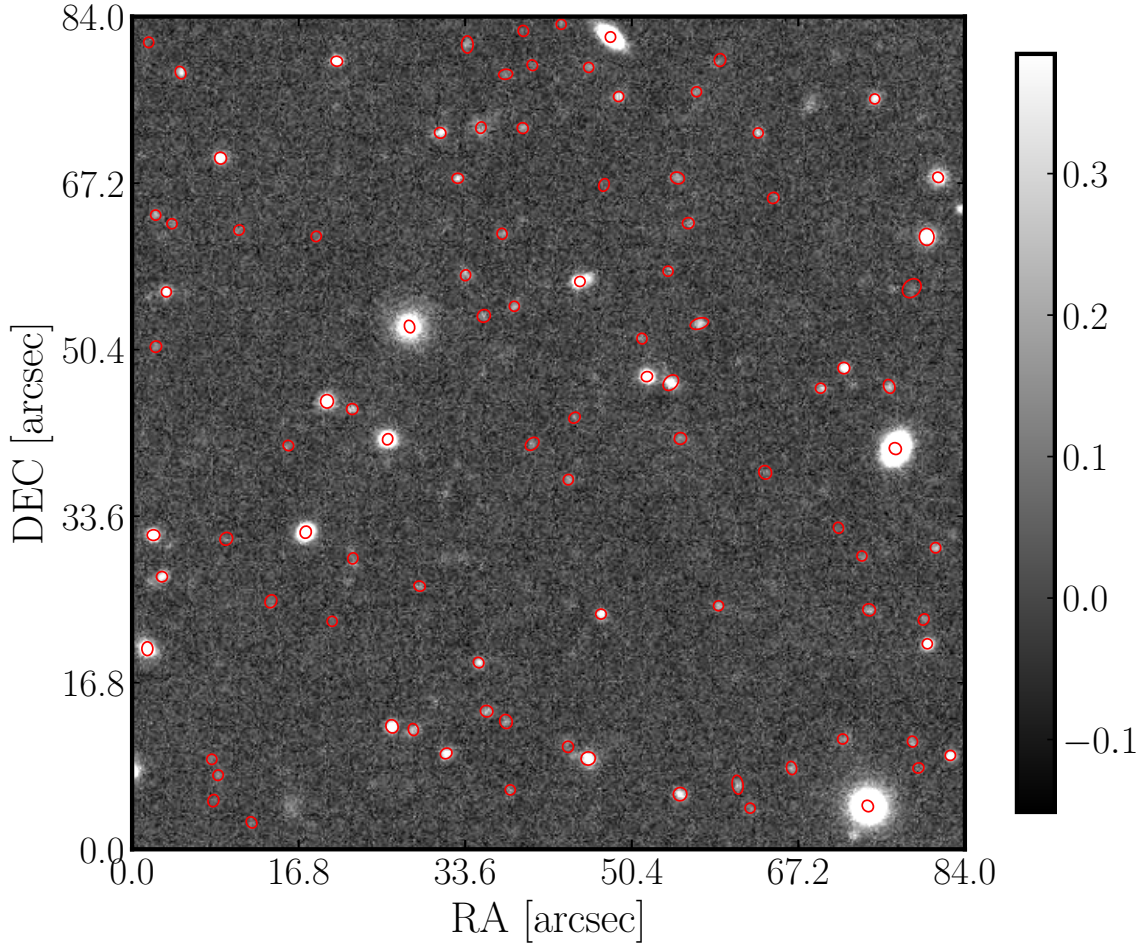


**Figure 3.** We present a 2 deg<sup>2</sup> image simulation used to evaluate the accuracy of our shear estimator. Details of the simulation setup are provided in Section 3.1. The red ellipses indicate the 2 $\sigma$  contours from Gaussian fits to the detected sources.

Common analytic functions extend neatly to quintuple numbers by performing a Taylor expansion in each infinitesimal direction and discarding second-order (or higher) terms. For instance:

**Exponentiation:**

$$\exp(q) = e^{q_0} \left( 1 + q_1 \epsilon_1 + q_2 \epsilon_2 + q_3 \epsilon_3 + q_4 \epsilon_4 \right). \quad (13)$$

**Power Functions:** For  $n \in \mathbb{R}$ , using the binomial expansion and discarding second-order (or higher) terms:

$$q^n = q_0^n + n q_0^{n-1} (q_1 \epsilon_1 + q_2 \epsilon_2 + q_3 \epsilon_3 + q_4 \epsilon_4). \quad (14)$$

This quintuple system offers a straightforward and systematic method for computing derivatives with respect to shear in the model-fitting operation, eliminating the need for symbolic differentiation or finite differences. By performing arithmetic directly on quintuple numbers, the partial derivatives with respect to shear naturally propagate through algebraic operations and function evaluations.

Concretely, we replace all input images in the model-fitting

code with images of quintuple numbers, denoted by

$$\mathcal{F}(\mathbf{x}) = \left( f_h(\mathbf{x}), \frac{\partial f_h(\mathbf{x})}{\partial \gamma_1}, \frac{\partial f_h(\mathbf{x})}{\partial \gamma_2}, J_1(\mathbf{x}), J_2(\mathbf{x}) \right). \quad (15)$$

where  $f_h$  is the smoothed renoised image,  $\frac{\partial f_h}{\partial \gamma_1}$ ,  $\frac{\partial f_h}{\partial \gamma_2}$ ,  $J_1$  and  $J_2$  are defined in equation (5) measured from the image. Additionally, we replace all arithmetic operations in the model-fitting code with those defined for quintuple numbers, as summarized in this subsection. As a result, the output of the model-fitting code is also a quintuple number. For instance, we denote the fitted ellipticity by  $\mathcal{E}_1$ :

$$\mathcal{E}_1 = \left( e_1, \frac{\partial e_1}{\partial \gamma_1}, \frac{\partial e_1}{\partial \gamma_2}, J_1^{e_1}, J_2^{e_1} \right). \quad (16)$$

Thus, the fitted ellipticity and its shear responses,  $\left( \frac{\partial e_1}{\partial \gamma_1}, \frac{\partial e_1}{\partial \gamma_2} \right)$  are automatically included in the quintuple output. The last two dimensions in the quintuple number output  $\mathcal{E}_1$  can be used to change the reference point that of the shear distortion.

Finally, the shear can be estimated as

$$\begin{aligned}\hat{\gamma}_1 &= \langle e_1 \rangle \left/ \left\langle \frac{\partial e_1}{\partial \gamma_1} \right\rangle \right., \\ \hat{\gamma}_2 &= \langle e_2 \rangle \left/ \left\langle \frac{\partial e_2}{\partial \gamma_2} \right\rangle \right.\end{aligned}\quad (17)$$

Even though we only use the first-order shear response, the estimated shear is accurate to the second order of shear since the second order of shear  $\gamma_{1,2}^2$  has different spin number to the galaxy shape  $\bar{\gamma}_{1,2}$ . Therefore, we have

$$\hat{\gamma}_{1,2} = \gamma_{1,2} + \mathcal{O}(\gamma^3). \quad (18)$$

## 2.4 Model Fitting

In this paper, we implement a simple Gaussian model to fit galaxy shapes, sizes, and fluxes, and demonstrate that our quintuple number system enables accurate propagation of the shear response through the model-fitting process. More sophisticated multi-component fitting approaches (e.g., *Euclid Collaboration et al. (2024)*) will be explored in a future publication.

We model the object as an elliptical 2D Gaussian with major axis length  $a_1$ , minor axis length  $a_2$ , and orientation angle  $\theta$ . The covariance matrix of the original Gaussian is:

$$\Sigma = Q \begin{pmatrix} a_1^2 & 0 \\ 0 & a_2^2 \end{pmatrix} Q^\top, \quad \text{where } Q = \begin{pmatrix} \cos \theta & -\sin \theta \\ \sin \theta & \cos \theta \end{pmatrix} \quad (19)$$

s the rotation matrix corresponding to an angle  $\theta$ .

Since the galaxy model is fit to the deconvolved image (see equation (4)), the Gaussian model must be convolved with the point spread function (PSF). We convolve this profile with the isotropic Gaussian PSF of width  $\sigma_h$ . The covariance matrix of the PSF is:

$$\Sigma_{\text{PSF}} = \sigma_h^2 I = \begin{pmatrix} \sigma_h^2 & 0 \\ 0 & \sigma_h^2 \end{pmatrix} \quad (20)$$

The resulting convolved Gaussian has a covariance matrix given by the sum:

$$\Sigma_o = \Sigma + \Sigma_{\text{PSF}}. \quad (21)$$

The PSF-convolved Gaussian is expressed as:

$$M(x, y) = \frac{F}{2\pi\sqrt{\det(\Sigma_o)}} \exp\left(-\frac{1}{2}\mathbf{x}'^T \Sigma_o^{-1} \mathbf{x}'\right), \quad (22)$$

where  $\mathbf{x}' = \mathbf{x} - \mathbf{x}_c$ , and  $\mathbf{x}_c$  is the center of the Gaussian. The galaxy shape is defined as

$$\begin{aligned}e_1 &= \frac{a_1^2 - a_2^2}{a_1^2 + a_2^2} \cos 2\theta, \\ e_2 &= \frac{a_1^2 - a_2^2}{a_1^2 + a_2^2} \sin 2\theta.\end{aligned}\quad (23)$$

We implement this Gaussian model-fitting algorithm with our quintuple number system and the shear estimation procedure consists of the following steps:

(i) **Quintuple Number Transformation:** Convert the exposure image into a *quintuple number image* following equations (4) and (5), where each pixel carries not only its intensity but also its shear response derivatives, enabling analytical propagation of shear effects.

(ii) **Galaxy Detection:** Identify galaxy candidates directly from the quintuple number image using the differentiable detection algorithm described in *Li et al. (2025)*. This step ensures that the detected objects already encode their response to shear.

(iii) **Gaussian Model Fitting:** For each detected object, perform independent Gaussian model fitting to estimate galaxy shape and flux parameters. The shear response is analytically propagated through the model-fitting process using the quintuple number formalism.

We simulate a set of intrinsically isotropic galaxies modeled with Sérsic profiles (*Sérsic 1963*) of varying indices, representing a range of realistic galaxy morphologies. Each galaxy is sheared by a small input distortion of  $\gamma_1 = 0.02$ . A simple Gaussian model-fitting algorithm is then applied to estimate both the galaxy shape and flux from the observed image. All galaxies have a half-light radius of  $0''.20$  and are convolved with a Moffat point spread function (PSF) (*Moffat 1969*), defined as

$$p(\mathbf{x}) = \left[ 1 + c \left( \frac{|\mathbf{x}|}{r_P} \right)^2 \right]^{-2.5}, \quad (24)$$

with parameters  $r_P$  and  $c$  chosen such that the full width at half maximum (FWHM) is  $0''.60$ , consistent with the median seeing of the HSC survey (*Li et al. 2022a*). Before measuring shapes and fluxes, we circularize the PSF by transforming it into an isotropic Gaussian with FWHM  $0''.70$ . The estimated shapes are then converted to shear using equation (18). To quantify the accuracy of shear recovery, we evaluate the standard multiplicative ( $m_{1,2}$ ) and additive ( $c_{1,2}$ ) bias parameters (*Huterer et al. 2006; Heymans et al. 2006*), defined through the relation:

$$\hat{\gamma}_{1,2} = (1 + m_{1,2}) \gamma_{1,2} + c_{1,2}. \quad (25)$$

The results are shown in Fig. 2. Despite fitting non-Gaussian galaxies with a Gaussian model—which introduces a flux bias of up to 15%—the resulting shear estimation biases remain below the 0.2% level relative to the input shear.

## 3 TEST ON IMAGE SIMULATION

### 3.1 Simulation

For our image simulations, we use the *descwl-shear-sims*<sup>1</sup> package, described in *Sheldon et al. (2023)*. This tool generates realistic synthetic galaxy images using the *GalSim* framework (*Rowe et al. 2015*). The outputs include background-subtracted, photometrically calibrated images, along with corresponding noise variance maps. Each simulation also includes a world coordinate system (WCS) and a point spread function (PSF) model.

To isolate the performance of the shear estimator under ideal conditions, we deliberately exclude sources of systematic error such as PSF modeling inaccuracies, noise misestimation, image warping artifacts, coaddition errors, and astrometric or photometric miscalibration. These effects are omitted to ensure that our tests reflect performance under well-controlled,

<sup>1</sup> <https://github.com/LSSTDESC/descwl-shear-sims>

coadded image conditions. While our current focus is on validation under these simplified circumstances, a complete shear calibration for real data will eventually require accounting for such imperfections.

All simulations include blended galaxy systems. A uniform shear is applied across each subfield, such that all galaxies within a given image experience the same lensing distortion. Both galaxy shapes and positions are transformed according to the applied shear, which takes values of  $\gamma_1 = \pm 0.02$  in our tests. Each simulation scenario comprises 5,000 subfields, each covering an area of  $0.036, \text{deg}^2$ .

To suppress shape noise, we adopt the ring test method (Massey et al. 2007), pairing each subfield with a counterpart rotated by  $90^\circ$ . Additionally, we apply the shape noise cancellation technique proposed by Pujol et al. (2019), which further reduces uncertainty in shear measurements arising from intrinsic galaxy shape dispersion and measurement noise. Simulations assume a circular Moffat PSF as defined in equation (24) with HSC seeing size FWHM equals  $0''.60$  (Li et al. 2022a), and we refer readers to Li et al. (2025) for tests with anisotropic PSFs.

To approximate the effect of residual Poisson noise due to high sky background, Gaussian noise is added after background subtraction. Noise levels are estimated using the `WeakLensingDeblending`<sup>2</sup> package (Sanchez et al. 2021), which is configured according to LSST filter characteristics. After adding all relevant features and noise, images are normalized to a photometric zero point of 27.

Unless otherwise specified, we simulate coadded images in the “*i*” band using the HSC year 3 depth (Li et al. 2022a) as our standard configuration. The input galaxies are modeled with `WeakLensingDeblending` and include bulge, disk, and AGN components. Morphologies are consistent across bands, though flux and ellipticity can vary between components. The AGN is represented as a central point source. The raw source density is 240 galaxies per square arcminute, with an effective *i*-band AB magnitude limit of 27. Galaxies are uniformly distributed without accounting for clustering.

To reduce statistical noise in bias estimation, we make use of both  $90^\circ$  rotated galaxy pairs (Massey et al. 2007) and the shape noise suppression method from Pujol et al. (2019). An example of the simulation is shown in Fig. 3.

### 3.2 Result

We assess the accuracy of our Gaussian model fitting algorithm introduced in Section 2.4, which has been fully implemented using the quintuple number system introduced in Section 2.3. This quintuple number system enables the analytical propagation of shear responses through the model-fitting process by automatically tracking first-order derivatives with respect to shear distortions. The implementation allows us to evaluate how the measured galaxy shape, size, and flux respond to small changes in gravitational shear without relying on finite-difference approximations.

In addition to testing model fitting, we also reimplemented our Fixed kernel shear estimator (FPFS; Li et al. (2018, 2022b)) estimator within the same quintuple number framework. The FPFS method estimates shear using second-order

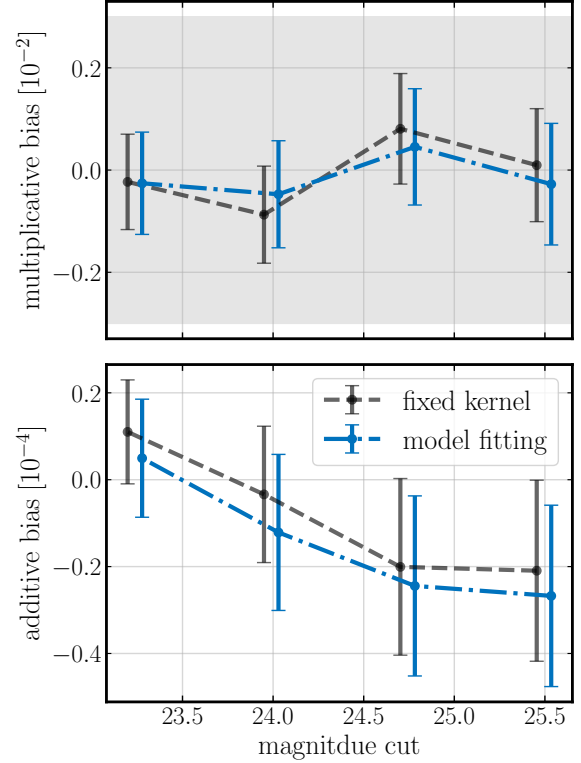


**Figure 4.** The multiplicative (upper panel) and additive bias (lower panel) as a function of magnitude cut. The black lines show the result for fixed-kernel shape estimator (FPFS) and the blue lines are for model-fitting code introduced in Section 2.4. The shaded region shows the requirement on the control of multiplicative bias in LSST Dark Energy Science Collaboration (The LSST Dark Energy Science Collaboration et al. 2018).

(Li et al. 2018) and fourth-order (Park et al. 2025) Shapelets (Refregier 2003; Massey & Refregier 2005) weight function applied to image pixels and it is optimized in Li et al. (2023). By integrating it into the quintuple system, we can now derive the shear response of FPFS estimators analytically and automatically, streamlining the calibration process while improving numerical robustness.

The figure illustrates the performance of both methods. The top panel shows the multiplicative bias ( $m_1$  in equation (25)) in the recovered shear estimates, while the bottom panel shows the corresponding additive bias ( $c_1$  in equation (25)). These biases are plotted as a function of magnitude cuts, where the magnitudes are computed from the fluxes returned by the model fitting.

For both the Gaussian model fitting and the FPFS method, the multiplicative biases remain well within the requirements set by the LSST Dark Energy Science Collaboration (The LSST Dark Energy Science Collaboration et al. 2018) for controlling shear calibration bias. Additionally, the additive biases are statistically consistent with zero, indicating that neither method introduces significant directional systematics into the shear measurements.

<sup>2</sup> <https://github.com/LSSTDESC/WeakLensingDeblending>

#### 4 SUMMARY AND OUTLOOK

In this paper, we have extended the **AnaCal** formalism to enable analytical shear response calculations for galaxy model fitting. By introducing the *quintuple number system*, a commutative ring inspired by dual numbers from automatic differentiation, we developed a method that can automatically propagate shear response information from image pixels to model-fit parameters, such as galaxy flux, shape, and size. This advancement allows us to analytically evaluate how small shear distortions impact the outcomes of model fitting, removing the need for finite differencing or image perturbation techniques.

We implemented a Gaussian model-fitting pipeline fully integrated with the quintuple number system, allowing us to derive shear responses alongside best-fit parameters in a single, automated process. Additionally, we reimplemented our **FPFS** estimator within the same algebraic system. This enabled the **FPFS** method, which uses a fixed Gaussian kernel for shear estimation, to inherit automatic shear response derivation, thus benefiting from the same analytical framework.

We validated both the Gaussian model-fitting estimator and the **FPFS** estimator using realistic image simulations covering  $180 \text{ deg}^2$  of sky with observing conditions modeled after the Hyper Suprime-Cam survey. The upper panel of our result figure shows the multiplicative bias for both methods, while the lower panel displays the corresponding additive bias. Both estimators achieve multiplicative biases well within the LSST shear bias requirements (i.e., below  $3 \times 10^{-3}$ ). The additive biases are consistent with zero, indicating that neither method introduces significant residual shear systematics.

Our results confirm that the quintuple number framework provides a robust, fully analytical, and computationally efficient foundation for future shear estimation pipelines. By bridging the pixel-level shear response to high-level galaxy parameter inference, this framework offers a promising path toward high-precision, survey-ready shear calibration.

In future work, we plan to extend the quintuple number framework to support more sophisticated model-fitting algorithms, including multi-component and Sérsic-based models that more accurately capture the diversity of galaxy morphologies (see e.g. Euclid Collaboration et al. (2024)). Incorporating these models may enhance the precision of shear response estimation, particularly for complex or blended systems. Additionally, we aim to integrate a deblending module within the quintuple number system, allowing analytical shear responses to be propagated through the deblending process (Sampson et al. 2024).

#### ACKNOWLEDGEMENTS

This paper makes use of software developed for the Vera C. Rubin Observatory. We thank the Vera C. Rubin Observatory for making their code available as free software at <http://dm.lsst.org>.

We thank the maintainers of NumPy (Harris et al. 2020), SciPy (Virtanen et al. 2020), Matplotlib (Hunter 2007), GalSim (Rowe et al. 2015) and conda-forge (conda-forge community 2021) projects for their excellent open-source software and software distribution systems.

We thank Erin Sheldon, Alan Zhou, Rachel Mandelbaum, Matthew Becker and Scott Dodelson for useful discussions.

Xiangchong Li is an employee of Brookhaven Science Associates, LLC under Contract No. DE-SC0012704 with the U.S. Department of Energy.

#### DATA AVAILABILITY

The code used for this paper is publicly available on Github: <https://github.com/mr-superonion/AnaCal/tree/v0.1.6>

#### REFERENCES

- Akeson R., et al., 2019, *arXiv e-prints*, p. [arXiv:1902.05569](#)
- Bartelmann M., Schneider P., 2001, *Physics Reports*, 340, 291
- Berlfein F., Mandelbaum R., Li X., Zhang T., Dodelson S., Markovic K., 2025, *arXiv e-prints*, p. [arXiv:2505.00093](#)
- Bernstein G. M., Armstrong R., 2014, *MNRAS*, 438, 1880
- Bernstein G. M., Armstrong R., Krawiec C., March M. C., 2016, *MNRAS*, 459, 4467
- Euclid Collaboration et al., 2024, *A&A*, 691, A319
- Gunes Baydin A., Pearlmutter B. A., Andreyevich Radul A., Siskind J. M., 2015, *arXiv e-prints*, p. [arXiv:1502.05767](#)
- Harris C. R., et al., 2020, *Nature*, 585, 357
- Heymans C., et al., 2006, *MNRAS*, 368, 1323
- Huff E., Mandelbaum R., 2017, preprint, ([arXiv:1702.02600](#))
- Hunter J. D., 2007, *Computing in Science and Engineering*, 9, 90
- Huterer D., Takada M., Bernstein G., Jain B., 2006, *MNRAS*, 366, 101
- Ivezić Ž., et al., 2019, *ApJ*, 873, 111
- Kilbinger M., 2015, *Reports on Progress in Physics*, 78, 086901
- Laureijs R., et al., 2011, preprint, ([arXiv:1110.3193](#))
- Li X., Mandelbaum R., 2023, *MNRAS*, 521, 4904
- Li X., Katayama N., Oguri M., More S., 2018, *MNRAS*, 481, 4445
- Li X., et al., 2022a, *PASJ*, 74, 421
- Li X., Li Y., Massey R., 2022b, *MNRAS*, 511, 4850
- Li X., Mandelbaum R., Jarvis M., Li Y., Park A., Zhang T., 2023, *MNRAS*,
- Li X., Mandelbaum R., Jarvis M., Li Y., Park A., Zhang T., 2024, *MNRAS*, 527, 10388
- Li X., Mandelbaum R., The LSST Dark Energy Science Collaboration 2025, *MNRAS*, 536, 3663
- MacCrann N., et al., 2022, *MNRAS*, 509, 3371
- Mandelbaum R., 2018, *ARA&A*, 56, 393
- Massey R., Refregier A., 2005, *MNRAS*, 363, 197
- Massey R., et al., 2007, *MNRAS*, 376, 13
- Massey R., et al., 2013, *MNRAS*, 429, 661
- Moffat A. F. J., 1969, *A&A*, 3, 455
- Park A., Li X., Mandelbaum R., 2025, *MNRAS*, 537, 507
- Peebles P. J., Ratra B., 2003, *Reviews of Modern Physics*, 75, 559
- Pujol A., Kilbinger M., Sureau F., Bobin J., 2019, *A&A*, 621, A2
- Refregier A., 2003, *MNRAS*, 338, 35
- Rowe B. T. P., et al., 2015, *Astronomy and Computing*, 10, 121
- Sampson M. L., Melchior P., Ward C., Birmingham S., 2024, *Astronomy and Computing*, 49, 100875
- Sanchez J., Mendoza I., Kirkby D. P., Burchat P. R., LSST Dark Energy Science Collaboration 2021, *JCAP*, 2021, 043
- Sérsic J. L., 1963, Boletín de la Asociación Argentina de Astronomía La Plata Argentina, 6, 41
- Sheldon E. S., Huff E. M., 2017, *ApJ*, 841, 24
- Sheldon E. S., Becker M. R., MacCrann N., Jarvis M., 2020, *ApJ*, 902, 138
- Sheldon E. S., Becker M. R., Jarvis M., Armstrong R., LSST Dark Energy Science Collaboration 2023, *The Open Journal of Astrophysics*, 6, 17

- The LSST Dark Energy Science Collaboration et al., 2018, arXiv e-prints, p. [arXiv:1809.01669](#)
- Virtanen P., et al., 2020, *Nature Methods*, **17**, 261
- Zhang J., 2008, *MNRAS*, **383**, 113
- Zhang Z., Sheldon E. S., Becker M. R., 2023a, *The Open Journal of Astrophysics*, **6**, 16
- Zhang T., et al., 2023b, *MNRAS*, **525**, 2441
- conda-forge community 2021, The conda-forge Project: Community-based Software Distribution Built on the conda Package Format and Ecosystem, [doi:10.5281/zenodo.4774217](#), <https://doi.org/10.5281/zenodo.4774217>